IN-24-TM

Kinetics of Cyclic Oxidation and Cracking and Finite Element Analysis of MA956 and Sapphire/MA956 Composite System

KANG N. LEE, VINOD K. ARYA, GARY R. HALFORD, and CHARLES A. BARRETT

Sapphire fiber-reinforced MA956 composites hold promise for significant weight savings and increased high-temperature structural capability, as compared to unreinforced MA956. As part of an overall assessment of the high-temperature characteristics of this material system, cyclic oxidation behavior was studied at 1093 °C and 1204 °C. Initially, both sets of coupons exhibited parabolic oxidation kinetics. Later, monolithic MA956 exhibited spallation and a linear weight loss, whereas the composite showed a linear weight gain without spallation. Weight loss of the monolithic MA956 resulted from the linking of a multiplicity of randomly oriented and closely spaced surface cracks that facilitated ready spallation. By contrast, cracking of the composite's oxide layer was nonintersecting and aligned nominally parallel with the orientation of the subsurface reinforcing fibers. Oxidative lifetime of monolithic MA956 was projected from the observed oxidation kinetics. Linear elastic, finite element continuum, and micromechanics analyses were performed on coupons of the monolithic and composite materials. Results of the analyses qualitatively agreed well with the observed oxide cracking and spallation behavior of both the MA956 and the Sapphire/MA956 composite coupons.

NASA-TM-112757

I. INTRODUCTION

THERE is considerable interest to increase the maximum operating temperature of heat engines above those using today's conventional materials. Fiber-reinforced metal-matrix composites (MMCs) have the potential for increased temperature capability because fibers can provide high material strength and creep resistance over long exposure time at high temperatures. The MMCs also promise significant weight savings because of high specific strength and modulus.

FeCrAlY- and NiCrAlY-based alloys are promising MMC matrix materials for high-temperature applications. FeCrAlY-based, oxide dispersion strengthened (ODS) superalloys show excellent oxidation resistance but reduced high-temperature strength, as compared to NiCrAlY-based superalloys.[1,2] Therefore, FeCrAlY-based ODS superalloys are of interest for heat exchanger tubes, sheet materials in combustion chambers, and burner nozzles.[3] The excellent oxidation resistance of FeCrAlY-based ODS superalloys having about 5 wt pct Al, such as MA956, is due to the formation of adherent and slow-growing alumina scale (α-Al_2O_3). The excellent adherence of the scale is due to the presence of small amounts of yttrium oxide (Y_2O_3). Several mechanisms by which yttrium oxide or other reactive metal oxides dramatically enhance the adherence of alumina scale have been reported.[4,5] Besides the enhancement of scale adherence, the presence of fine, stable, and uniformly distributed oxide particles gives ODS alloys improved creep resistance by acting as barriers to dislocation motion.

One of the key issues in composite materials is the fiber/matrix interface. The interface must be chemically stable[6] and possess a bond strength great enough to prevent oxidation penetration,[7] while allowing load transfer between the matrix and fibers.[8] The latter is difficult to achieve; too weak a bond may lead to oxidation penetration,[7,9] whereas too strong a bond, coupled with a coefficient of thermal expansion (CTE) mismatch, may lead to thermal fatigue cracking of the matrix.

The purpose of this article is to report the cyclic oxidation and resulting cracking behavior of MA956 and a Sapphire fiber-reinforced MA956 composite at maximum temperatures of 1093 °C or 1204 °C. Finite element analyses were conducted to understand the cracking behavior.

II. EXPERIMENT

MA956 and Sapphire/MA956 composites were produced in the form of 15 × 15 × 0.15-cm plates.* The Sapphire/MA956 composites consisted of six unidirectional plies of fibers with a fiber volume of 35 pct. The nominal composition of MA956 is shown in Table I. Oxidation coupons with a typical dimension of 2.5 × 1.3 × 0.15 cm were machined from the plates, with fibers oriented parallel to the short side (1.3 cm) of coupons. The fiber ends of the oxidation coupons were left exposed. Specimens were polished through 600-grit SiC abrasive paper, cleaned in an ultrasonic cleaner, and rinsed in acetone. Specimens were then tested under cyclic oxidation conditions at maximum temperatures of 1093 °C and 1204 °C. Each cycle consisted of 1 hour at maximum temperature, rapid cooling to room temperature (RT) in static air, and at least 20 minutes at RT. Specimens were weighed at selected intervals to determine the oxidation kinetics. Post-test examination was conducted using routine characterization methods, such as

*Supplied by Pratt and Whitney, West Palm Beach, FL.

KANG N. LEE, Resident Research Associate at the NASA-Lewis Research Center, Cleveland State University, Cleveland, OH 44115, VINOD K. ARYA, Resident Research Associate at the NASA-Lewis Research Center, University of Akron, Akron, OH 44325, GARY R. HALFORD, Senior Scientist, and CHARLES A. BARRETT, Staff Engineer, are with the NASA-Lewis Research Center, Cleveland, OH 44135.

Manuscript submitted August 29, 1995.

Table I. Nominal Composition of MA956 (Weight Percent)

Fe	Cr	Al	Ti	Y_2O_3
74.5	20	4.5	0.5	0.5

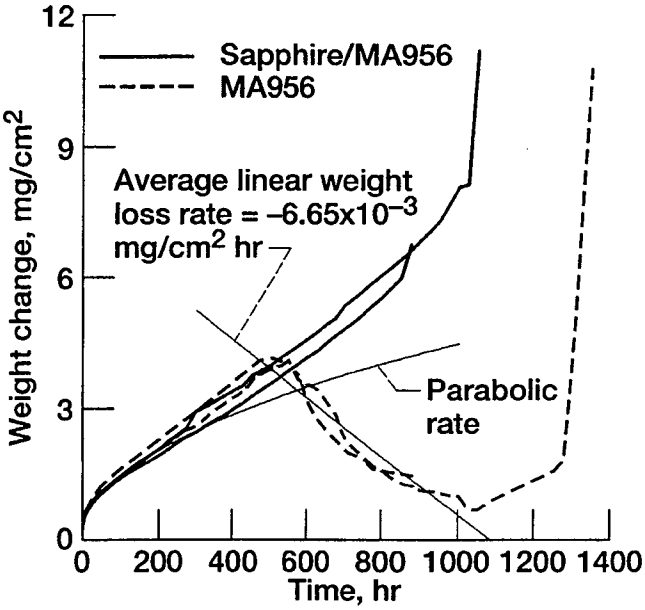

Fig. 1—The oxidation kinetics of MA956 and Sapphire/MA956 composite at 1204 °C with 1-h cycle.

optical microscopy, scanning electron microscopy (SEM), energy dispersive spectroscopy (EDS), and X-ray diffraction (XRD).

III. RESULTS AND DISCUSSION OF OXIDATION KINETICS

A. *Oxidation at 1204 °C*

Figure 1 shows the oxidation kinetics of MA956 and Sapphire/MA956 composite at 1204 °C. MA956 exhibited four kinetics stages: (1) parabolic (0 to 200 hours), (2) approximately linear weight gain (200 to 500 hours), (3) weight loss (500 to 1000 hours), and (4) breakaway (1000 hours). Stages 1 and 3 are typical of alumina-forming alloys (paralinear oxidation). Sapphire/MA956 composite exhibited three kinetics stages: (1) parabolic (0 to 200 hours), (2) approximately linear weight gain (200 to 1000 hours), and (3) breakaway (1000 hours). Note that the weight-loss period was absent in the composite. According to XRD at various intervals, the oxide scale was predominantly Al_2O_3, with a trace amount of Fe_2O_3 during the parabolic and the linear weight-gain period. The Fe_2O_3 presumably formed during the transient oxidation before the parabolic oxidation was established.

1. *MA956*

During the parabolic oxidation stage, minor scale spallation was observed at the edges and corners where the stress was higher than the flat surface, due to the geometrical constraint. However, the amount of spallation was so small that the parabolic oxidation rate was maintained. It is generally agreed that the rate-controlling step during parabolic growth of alumina scale is grain boundary diffusion of oxygen through the alumina scale.[10] During the linear weight-gain stage, some scale cracking began to appear on the flat surface. The scale cracking enhanced the oxidation weight gain compared with the weight gain in the case of crack-free scale, presumably due to the exposed bare metal surface and the shorter diffusion path for oxygen at the crack tips. As a result, the specific weight gain based on the nominal surface area, *i.e.*, total weight gain/nominal surface area, increased linearly with time, although the diffusion of oxygen through the scale was still the rate-limiting step. Figures 2(a) and (b) show the oxidized surface after 600 and 1275 hours, respectively. Significant cracking and scale spallation were observed after 600 hours. By this time, the weight loss due to the scale spallation became the rate-limiting step for the overall weight change, which led to the weight-loss stage. The cracks and spallation were randomly distributed over the entire surface. After 1275 hours, massive cracking and scale spallation occurred, and patches of black oxide began to appear (Figure 2(b)). X-ray diffraction showed that the black oxide was $(Fe,Cr)_2O_3$. According to the EDS analysis, the black oxide contained both Fe and Cr as the major constituents, consistent with the XRD. At this stage, the formation of $(Fe,Cr)_2O_3$ became the rate-limiting step, which triggered the breakaway oxidation, due to its rapid growth rate. The

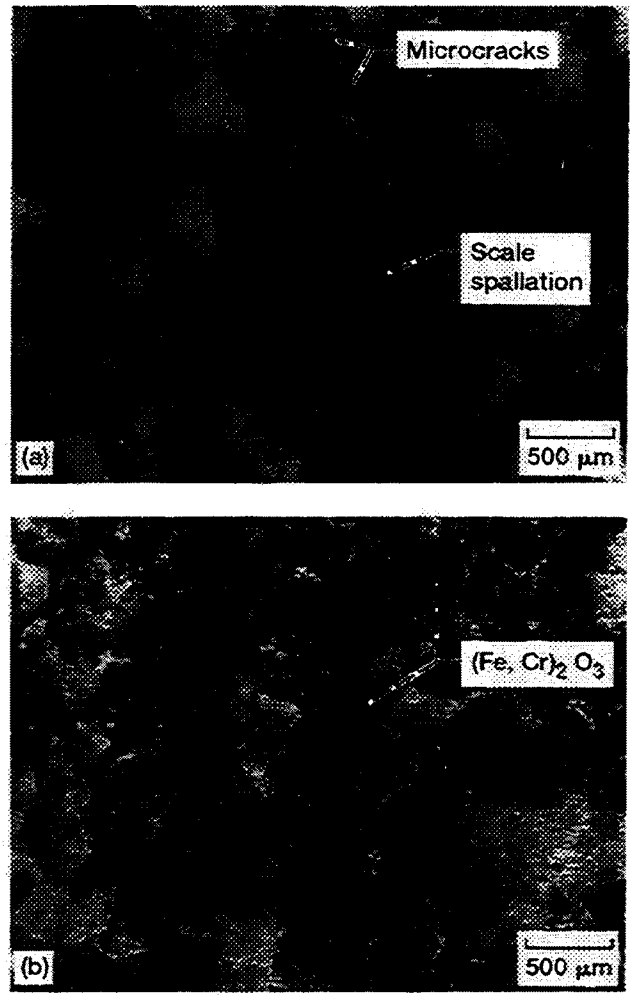

Fig. 2—The surface of oxide scale on MA956 at 1204 °C with 1-h cycle: (*a*) 600 cycles and (*b*) 1275 cycles.

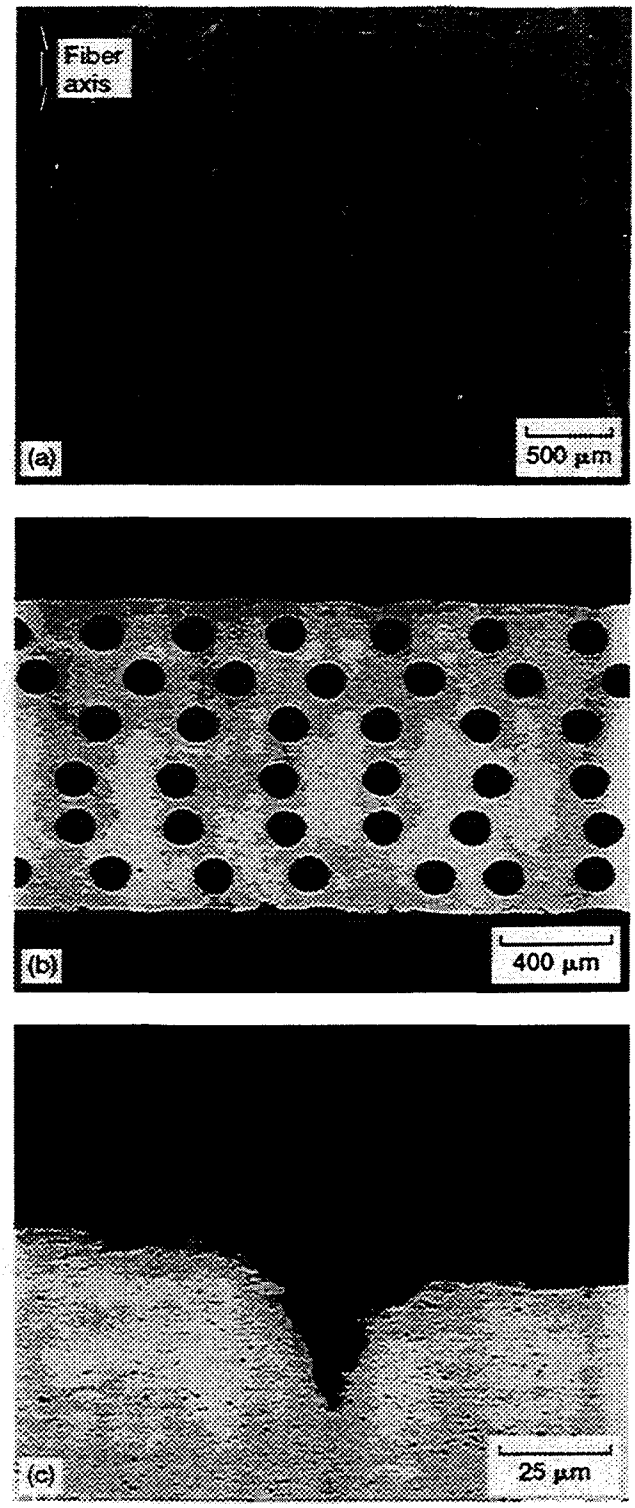

Fig. 3—The oxide scale on Sapphire/MA956 composite after 250 1-h cycles at 1204 °C: (*a*) surface and (*b*) and (*c*) cross section.

$(Fe,Cr)_2O_3$ first formed at the corners where the Al consumption rate was most rapid.

2. *Sapphire/MA956 composite*

As in MA956, minor scale spallation was observed at the edges and corners during the parabolic oxidation stage. During the linear weight-gain stage, massive cracks parallel to the fiber axis began to develop in a fairly uniform pattern. However, no appreciable scale spallation was observed, explaining the absence of the weight-loss period. Cracks were first observed after around 200 hours, when the kinetics deviated from the parabolic to the linear weight-gain stage. Again, as in MA956, this deviation from the parabolic oxidation to the linear weight gain was ascribed to the enhanced weight gain due to the exposed bare metal surface and the shorter diffusion path at the crack tips. Figures 3(a) through (c) show the oxidized surface and the cross section of oxide scale at 250 hours. Note that cracks are parallel to the fiber axis (Figure 3(a)), and are located approximately between two fibers of the outer ply (Figure 3(b)). Also note that cracks have penetrated into the alloy substrate (Figure 3(b)). As described previously, this penetration created new surface for oxidation, leading to the transition to the linear weight-gain stage. Figures 4(a) through (c) show the surface and the cross section of oxide scale at 1075 hours. Note the progress of the cracking across the entire surface (Figure 4(a)) and the deep penetration into the substrate (Figures 4(b) and (c)). As in MA956, the formation of $(Fe,Cr)_2O_3$ became the rate-limiting step after 1000 hours, leading to the breakaway oxidation.

Figures 5(a) and (b) and Figures 6(a) and (b) show cross sections of the composite parallel to the fiber axis after 250 and 1075 hours, respectively. Some limited penetration of oxidation along the fiber/matrix interface was observed at the exposed fiber ends (Figures 5(a) and 6(a)). However, the rest of the matrix was intact from oxidation (Figures 5(b) and 6(b)), indicative of a strong bonding between the fibers and matrix. Cyclic oxidation of a Al_2O_3/FeCrAlY composite processed by a different technique showed significant oxidation along the fiber/matrix interface at 1000 °C due to a weak fiber/matrix bond.[9] The weak fiber/matrix bond presumably resulted in a stress state different from the present study, and thus caused a different cracking behavior, *i.e.*, cracks both parallel and perpendicular to the fibers.[9] Different processing techniques can produce different fiber/matrix bond strength.[7] A strong fiber/matrix bonding is desirable from the oxidation point of view. However, it can cause a high thermal stress when coupled with a large interfacial CTE mismatch (Table II).

Figures 7(a) through (c) show exposed fiber ends after 5, 150, and 1025 hours, respectively. Bright halos appear around the fiber ends after 5 hours, which were areas of exposed bare metal as a result of scale spallation (Figure 7(a)). The scale spallation around the fibers is due to the CTE mismatch between the fibers and the matrix. The process of spallation and reforming of oxide repeated itself as the thermal cycling continued. Eventually, the matrix around the fibers cracked due to the thermal fatigue (Figures 7(b) and (c)) .

B. *Oxidation at 1093 °C*

Figure 8 shows the oxidation kinetics of MA956 and Sapphire/MA956 composite at 1093 °C. The agreement in parabolic rate between the two coupons is fairly good up to 400 hours. At around 400 hours, the oxidation rate of Sapphire/MA956 composite deviated to linear kinetics, while that of MA956 slowed down slightly. Cracking of the oxide scale similar to that observed at 1204 °C began to appear on the composite during the transition. Similar

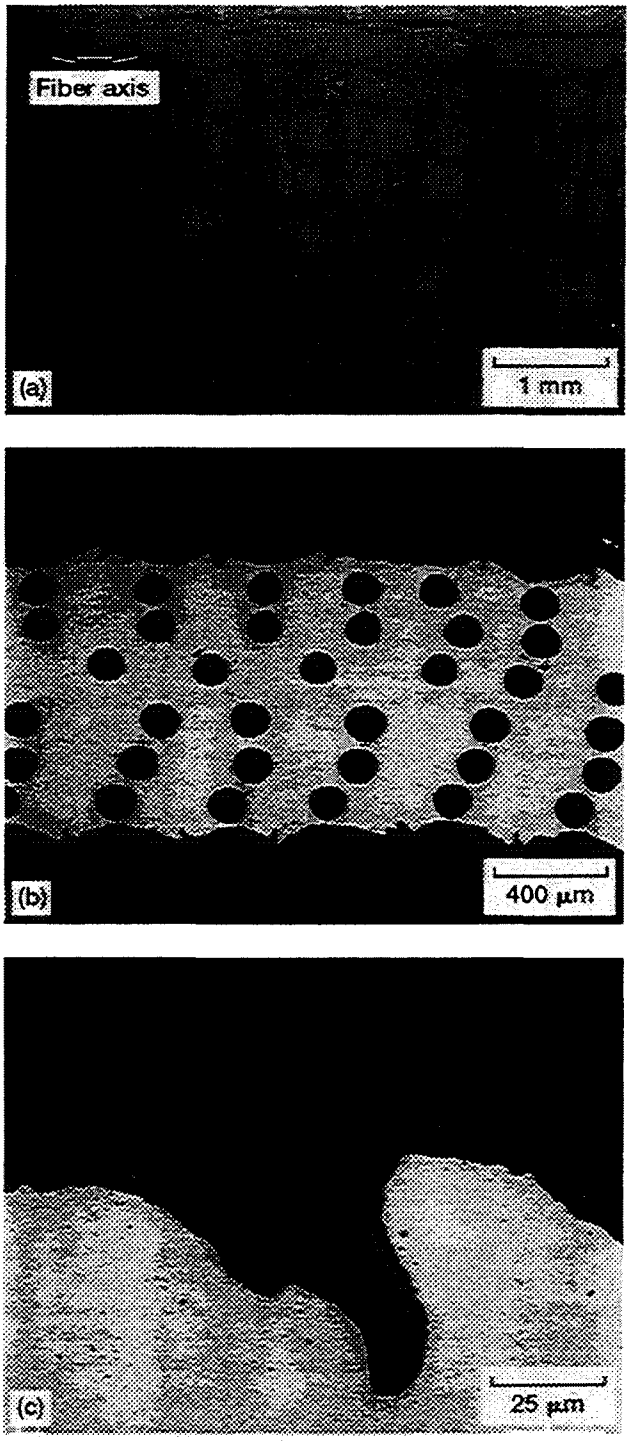

Fig. 4—The oxide scale on Sapphire/MA956 composite after 1075 1-h cycles at 1204 °C: (*a*) surface and (*b*) and (*c*) cross section.

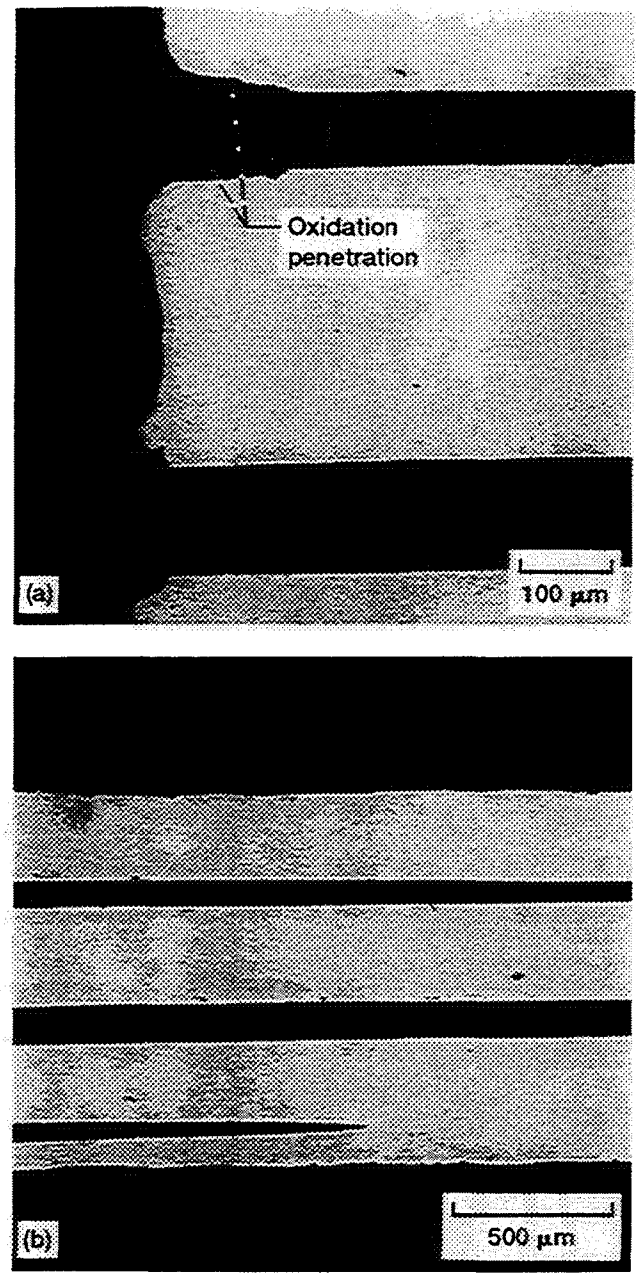

Fig. 5—The cross section of Sapphire/MA956 composite parallel to the fiber axis after 250 1-h cycles at 1204 °C: (*a*) around the exposed fiber ends and (*b*) away from the exposed fiber ends.

weight change patterns shown in Figure 1 are expected for both samples, although the time for each phase will be greatly extended.

C. *Oxidative lifetime projection of MA956*

Aluminum concentration profiles across the alloy thickness, during the oxidation of MA956 at 1200 °C, were practically flat with no clear Al concentration gradient beneath the oxide scale.[11,12] This uniform distribution of Al allows the estimation of Al concentration at a given time, which enables one to project the oxidative lifetime of MA956. Several assumptions were made for the calculation. First, during the weight-gain period (parabolic and linear weight gain), the Al consumption rate was calculated from the stoichiometry of the oxidation reaction, *i.e.*, $2Al + 3/2O_2 = Al_2O_3$, in conjunction with the weight-gain data. Extrapolated parabolic weight gain (Figure 1) was used for the linear weight-gain period to simplify the calculation. This is justified considering the approximate nature of the calculation. Second, during the weight-loss period, the rate of Al loss, $dW(Al)/dt$, was taken from the average slope of the weight-loss curve, and was assumed to be applicable as an approximation for the entire protective life of a specimen.[13,14] Third, a plate with infinite width and finite thick-

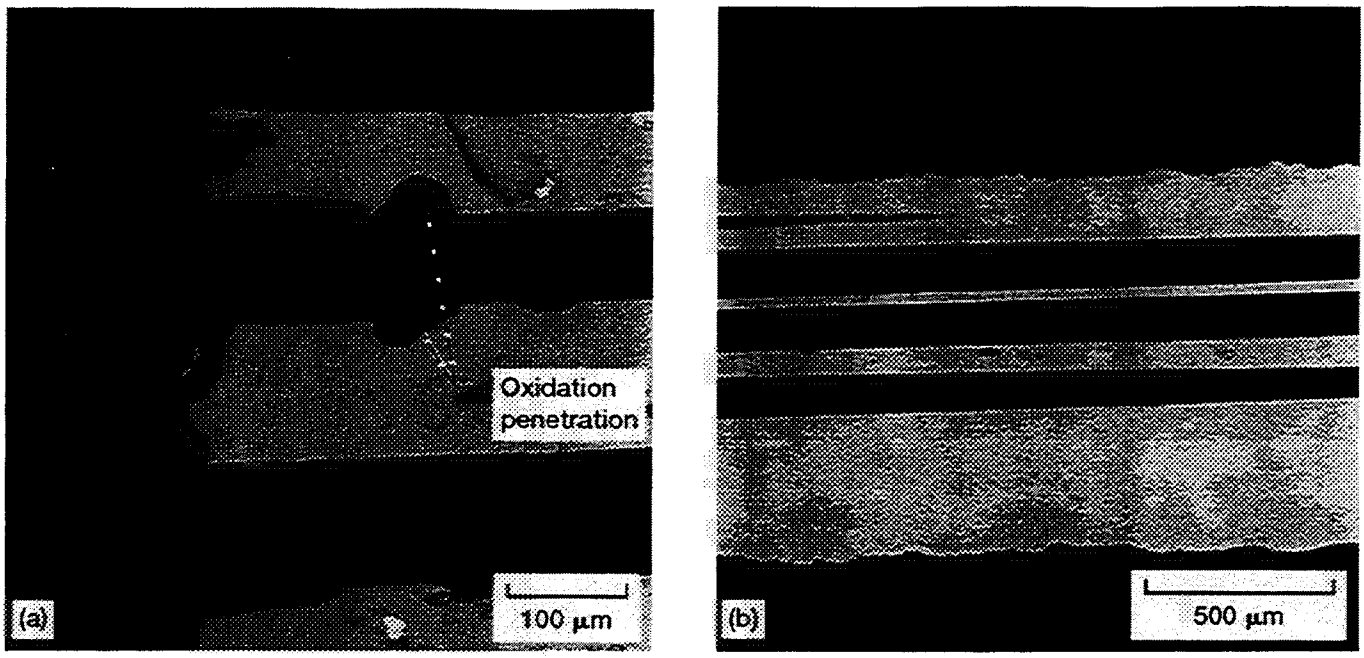

Fig. 6—The cross section of Sapphire/MA956 composite parallel to the fiber axis after 1075 1-h cycles at 1204 °C: (*a*) around the exposed fiber ends and (*b*) away from the exposed fiber ends.

Table II. Mechanical Properties of Constituents

Material	Property	Temperature 20.0	240.0	460.0	680.0	900.0	1120.0	1230.0
Fiber	E	451,070	443,070	434,730	426,040	416,870	407,220	402,185
	ν	0.2197	0.2165	0.2131	0.2095	0.2058	0.2018	0.1997
	α	0.7137	0.7643	0.8219	0.8881	0.9653	1.0559	1.1074
Matrix	E	211,400	188,578	166,376	145,000	124,385	104,600	95,080
	ν	0.2996	0.2872	0.2741	0.2605	0.2461	0.2308	0.2227
	α	0.9173	1.0595	1.2400	1.4747	1.7887	2.2230	2.5074
Oxide	E	458,310	437,625	416,940	396,255	375,570	354,885	344,540
	ν	0.2500	0.2639	0.2779	0.2919	0.3170	0.3570	0.3770
	α	0.5400	0.7500	0.8200	0.8800	0.9400	0.9900	1.0300

Units: Temperature in °C, E in MPa, and α in (10^{-5} °C^{-1}).

E: Young's modulus, ν: Poisson's ratio, and α: coefficient of thermal expansion.

ness was assumed, so that oxidation at the edges was neglected. Fourth, the density of the alloy was assumed to remain constant throughout the protective life (7.2 mg/cm^2). Using these assumptions, the Al consumption rate and the resulting Al content in MA956 during the course of oxidation were calculated from the kinetics data. One key piece of information necessary for the projection of oxidative lifetime is the concentration of Al at the end of oxidative life (*i.e.*, the critical aluminum concentration,[15] C_{Al}*). The C_{Al}* of MA956 calculated from Figure 1 was about 2.7 wt pct, substantially higher than that reported by Quadakkers *et al.* (1.3 wt pct).[11,12] The reason for the discrepancy is not understood at this point. Because the oxidative lifetime is dependent on the amount of aluminum available, which in turn is dependent on the alloy thickness, it is useful to plot the oxidative lifetime as a function of the alloy thickness. Figure 9 is a plot of the estimated lifetime *vs* alloy thickness for MA956 (C_{Al}* of 2.7 wt pct was used in this calculation). Solid lines are the projected lifetime for paralinear oxidation behavior. For a comparison, the lifetime for an ideal case, when parabolic oxidation continues for the entire protective life, is shown as dotted lines. Note that the lifetime in paralinear oxidation deviates negatively from that in parabolic oxidation when the alloy thickness is larger than 0.06 cm. This deviation is due to the transition of oxidation mode from parabolic to linear weight loss, and the resulting increased Al consumption rate.

IV. FINITE ELEMENT ANALYSES

This section presents the results of elastic finite element analyses performed to understand the observed dissimilar cyclic oxidation cracking and spallation behavior of the MA956 and Sapphire/MA956 systems. Results being sought are qualitative, *i.e.*, the orientation and location of cyclic cracking in the oxide layer formed on both material systems. It was necessary to perform both continuum and micromechanical analyses. The continuum approach ad-

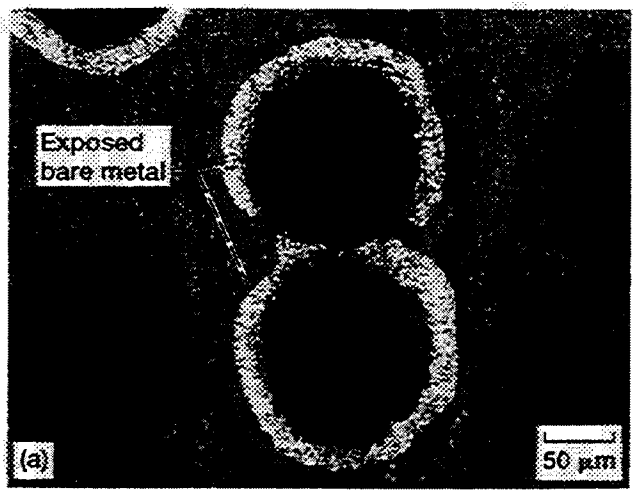

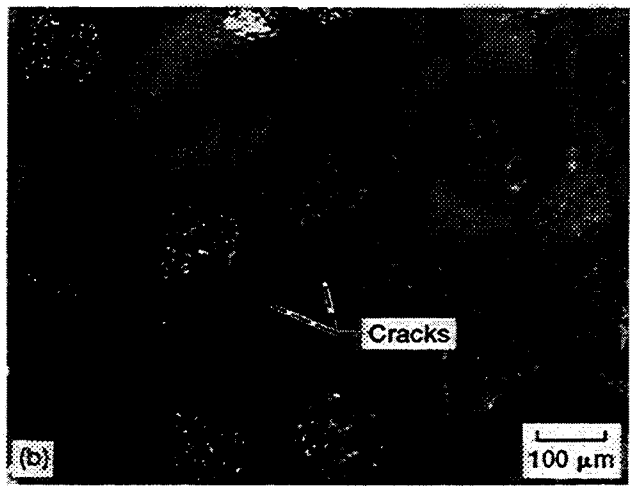

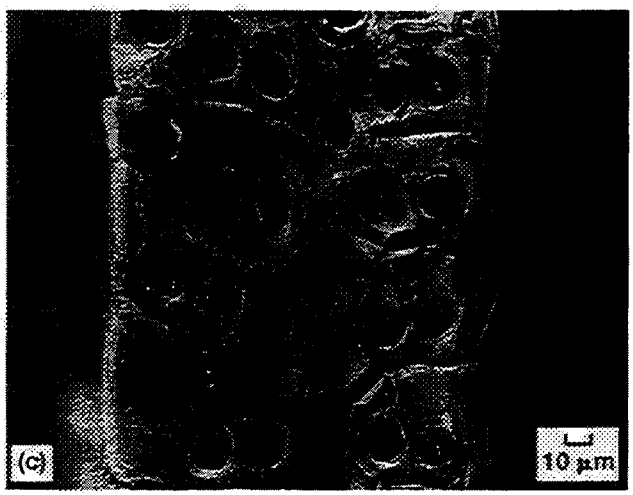

Fig. 7—The exposed fiber ends of Sapphire/MA956 composite at 1204 °C with 1-h cycle: (*a*) five cycles, (*b*) 150 cycles, and (*c*) 1025 cycles.

dressed the orientation of cracking and why the two systems differed so drastically. On the other hand, the micromechanics analyses of the composite system were required to understand why the oxide cracks formed parallel to the fibers and were located in the oxide layer immediately above each valley between adjoining fibers in the outermost ply. The pertinent temperature-dependent material

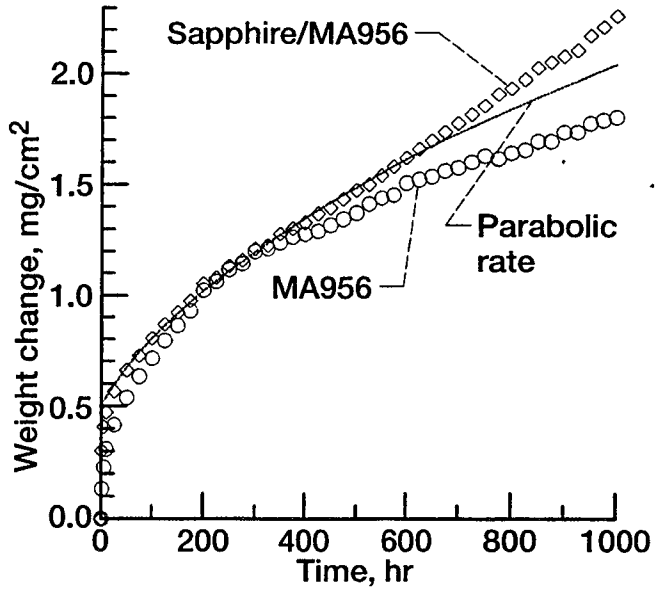

Fig. 8—The oxidation kinetics of MA956 and Sapphire/MA956 composites at 1093 °C with 1-h cycle.

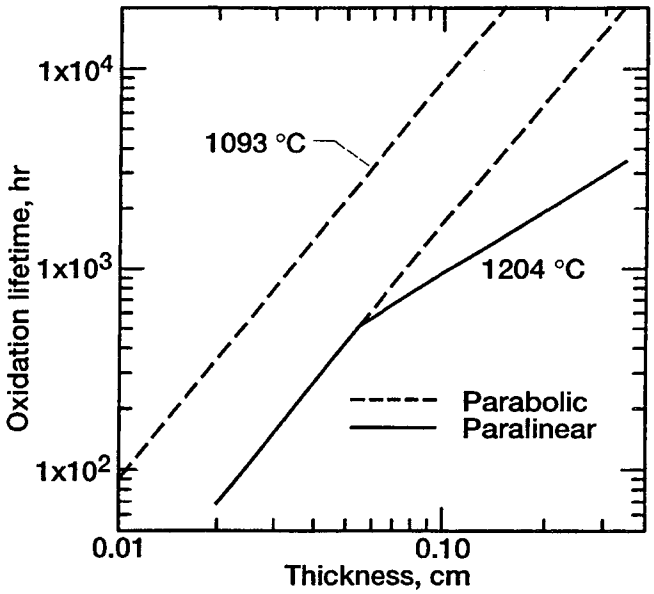

Fig. 9—The projected oxidative lifetime of MA956 *vs* alloy thickness.

properties of the constituent materials are given in Tables II and III. The discrete values listed were computed from published equations.[16,17] Details of the finite analyses and the pertinent results are subsequently discussed.

A. *Continuum Finite Element Analyses*

Only a small corner portion of the experimental plate (0.15 × 0.15 × 0.076 cm) needed to be modeled. The plate model is shown in Figure 10 and consists of 1440 solid, eight-noded, hexagonal finite elements with 1859 nodes. The surfaces exposed to oxidation are the top, right-hand end, and hidden back face. For the analyses, the thickness of the oxide layer was taken as 10 μm, *i.e.*, 1/76 the thickness of the substrate in the model. This thickness was selected because it corresponds to the thickness at which

Table III. Effective Properties of the Composite

Property	Temperature 20.0	240.0	460.0	680.0	900.0	1120.0	1230.0
E_{11}	290,480	272,560	252,220	237,740	220,915	204,505	196,440
E_{22}	264,770	241,880	218,920	195,820	172,650	149,410	137,760
ν_{12}	0.2733	0.2638	0.2540	0.2437	0.2328	0.2212	1.1074
ν_{23}	0.2818	0.2723	0.2622	0.2513	0.2396	0.2265	0.2195
ν_{31}	0.2491	0.2342	0.2181	0.2007	0.1819	0.1616	0.1509
G_{12}	103,425	94,460	85,360	76,330	67,160	58,055	53,575
G_{23}	103,290	95,080	86,340	78,260	69,640	60,880	56,470
G_{31}	103,425	94,460	85,360	76,330	67,160	58,055	53,575
α_{11}	0.8131	0.9011	1.0048	1.1279	1.4562	1.5300	1.0300
α_{22}	0.8401	0.9461	1.0075	1.2440	1.4606	1.7528	1.9404

Units: temperature in °C, G and E in MPa, and α in (10^{-5} °C^{-1}).

$E_{22} = E_{33}$, $\alpha_{22} = \alpha_{33}$, and G: shear modulus.

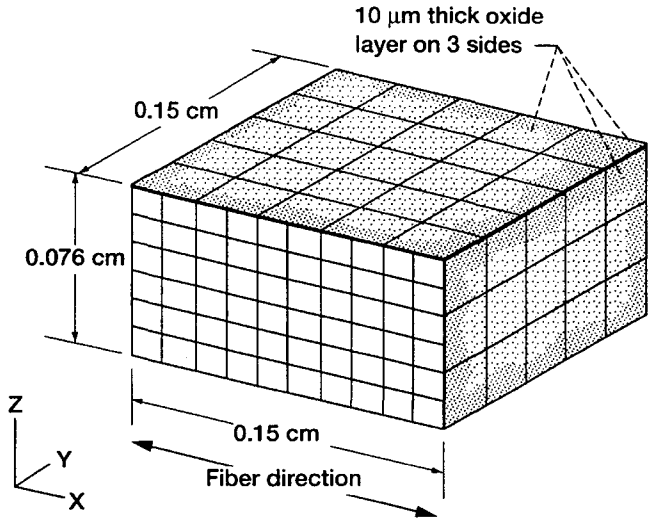

Fig. 10—The finite element model used for the continuum finite element analysis (1440 elements, 1859 nodes).

parabolic oxidation ends and linear begins. We will concentrate our attention on the top layer of oxide.

The continuum analyses were performed using the finite element program MARC.*[18] The temperature-dependent, effective orthotopic properties of the composite plate were generated using the program METCAN[19] and the properties of individual constituents. The computed composite properties are listed in Table III. Only elastic mechanical properties have been considered for the finite element analyses. Justification for the adequacy of this selection will become apparent as the analytic results are discussed. The imposed thermal loading consisted of uniformly heating (*i.e.*, imposing negligibly small thermal gradients) the model from 21 °C to 1204 °C. Some of the most important computed results sought from the finite element analyses are the magnitude and orientation of the cyclic ranges of mechanical strains imposed in the thin upper oxide layer by the much thicker, stronger substrate. These cyclic mechanical strain ranges are of interest because they are responsible for the observed oxide cracking and spallation. The mechanical strains result directly from the thermal expansion mismatch between the oxide and substrate.

The basic laws of mechanics that govern elastic superposition of stresses and strains can be used to show that the elastically calculated *range* of mechanical strain in the oxide is independent of the assumed magnitude of the initial residual stresses in the oxide and substrate. Consequently, the computationally simplifying assumption could be made that any residual stresses and strains within the substrate and oxide layer can be considered to be zero at 21 °C. This assumption is also justified in the ensuing discussion of analytic results. Upon heating to 1204 °C, the higher CTE of the substrate composite material (compared to the oxide) causes it to expand a greater amount than the oxide layer (which expands naturally on its own, but not by as much). Hence, the thicker, stronger substrate mechanically forces the thin initially adherent oxide layer to follow along and traverse the same displacement as the substrate. This causes the oxide to be mechanically strained in tension. Upon cooling, the oxide layer is mechanically strained in the compressive direction by the same amount that it had been stretched, *etc.* for continued thermal cycling. Hence, the *range* of elastically calculated mechanical strain experienced by the oxide is numerically equal to the magnitude of the tensile mechanical strain elastically computed for the initial heat-up portion of a cycle.

B. *Results of Continuum Analyses*

The calculated mechanical* strains induced throughout the model in the three coordinate directions by heating from 21 °C to 1204 °C are shown in Figure 11, along with the elastically calculated stresses in the x direction (*i.e.*, parallel to the fibers). Of greatest importance is the magnitude of the strain induced in the upper oxide layer. In the x direction, the strain is +0.00271. For repeated thermal cycling, this becomes the value of the cyclic strain range of the oxide in the x direction. Correspondingly, the x direction strain in the bulk of the substrate coupon is only −0.00097. In this direction, the magnitude of the oxide strain exceeds the sub-

*MARC is a trademark of MARC Analysis Research Corporation, Palo Alto, CA.

*Mechanical strain is the total strain minus thermal expansion strain (CTE times temperature change) and is further subdivided into elastic (stress/modulus of elasticity) and inelastic (width of stress-strain hysteresis loop at zero stress).

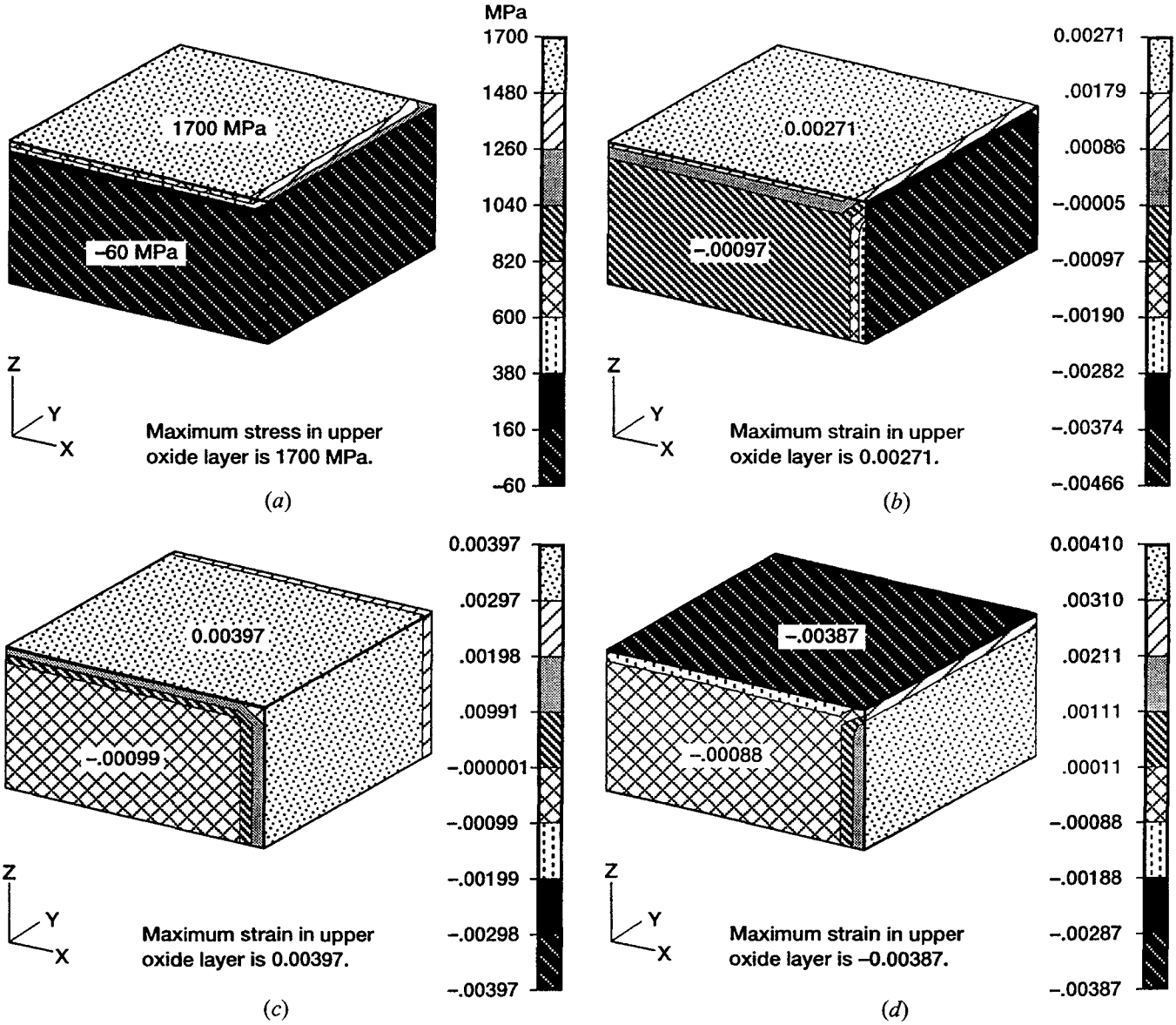

Fig. 11—The stress and mechanical strains produced in the oxide layer and the Sapphire/MA956 composite plate due to the CTE mismatch between the 10-mm-thick oxide (top, right-hand end, and back surface) and the composite substrate under thermal cycling from 21 °C to 1204 °C: (*a*) *x* stress, (*b*) mechanical *x* strain, (*c*) mechanical *y* strain, and (*d*) mechanical *z* strain.

strate strain by a factor of 27. This clearly shows that the thicker, stronger substrate is forcing the thin, weaker oxide layer to follow along in a slave/master relation.

Were the oxide to behave elastically, the induced stress in the *x* direction would be +1700 MPa (Figure 11(a)). Similarly high stresses were also elastically computed for the *y* and *z* directions. These stresses exceed literature values of the 0.2 pct offset yield strength for pristine Al_2O_3 oxide, implying significant inelastically induced in the oxide. Literature values range from as low as 60 MPa (single crystal[20]) to as high as 480 MPa (polycrystalline[21]) at temperatures in the range of 21 °C to 1204 °C. The oxide strength is nominally independent of temperature within these limits.

To assess the stress-strain response in the upper oxide layer under conditions of yielding, we adopt a cyclic stress-strain curve with elastic-perfectly plastic behavior. The assumed yield strength is taken as 480 MPa, although other values could be chosen without altering the quantitative end results being sought. A realistic approximation to the *x*-direction stress-strain hysteresis loop (0aebcde) is constructed in Figure 12 using the total strain range of 0.00271 computed from the elastic modeling. Because of yielding in tension on heating (0aeb), the stresses in the oxide become compressive upon cooling to 21 °C (bcd). A stable, repeating hysteresis loop is established after the first cycle. With the amount of inelastic deformation incurred, any residual stresses that might have been present initially would have been completely "washed out" and, hence, knowledge of their magnitudes would be unimportant to the current analyses. This phenomenon is illustrated in Figure 13(a) wherein three initial residual stresses are considered: 0 (zero), 0' (tensile), and 0" (compressive). The size and shape of the resultant hysteresis loop (bcde) are seen to be independent of the initial starting stress. Had the initial starting point of the analyses been at the highest temperature of 1204 °C, the resultant hysteresis loop (ghij) would

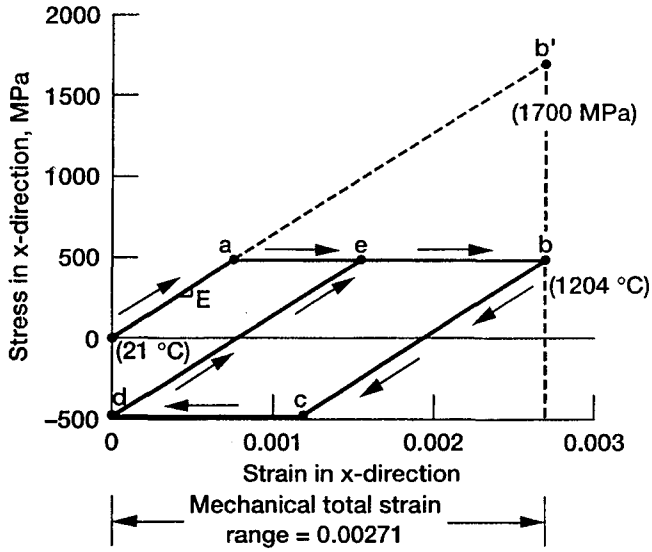

Fig. 12—Stress-strain hysteresis loop in the x direction in oxide in thermally cycled Sapphire/MA956 composite plate for elastic-perfectly plastic behavior; yield strength = 480 MPa.

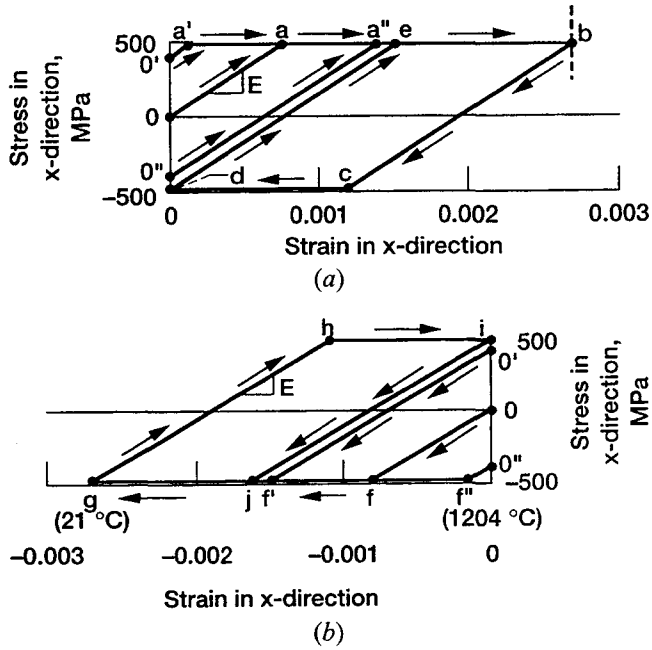

Fig. 13—Stress-strain hysteresis loops in x direction in oxide showing lack of influence of initial residual stresses: (a) starting at 21 °C and (b) starting at 1204 °C.

appear as shown in Figure 13(b). The only difference between the hysteresis loops of Figures 13(a) and (b) is a shift in the arbitrary zero strain starting point. It must be emphasized that an inelastic stress-strain analysis would not appreciably change the magnitude of the cyclic mechanical total strain range in the oxide layer.*

*For the current analyses, plastic flow in the oxide layer would lower the range of stress in both the oxide and substrate causing a *small increase* in the oxide mechanical strain range. The increase is a second-order effect amounting to just less than 10 pct; an amount far too small to alter the qualitative results sought herein.

The preceding cyclic stress-strain analysis considered only the x direction. Duplicate analyses could be performed

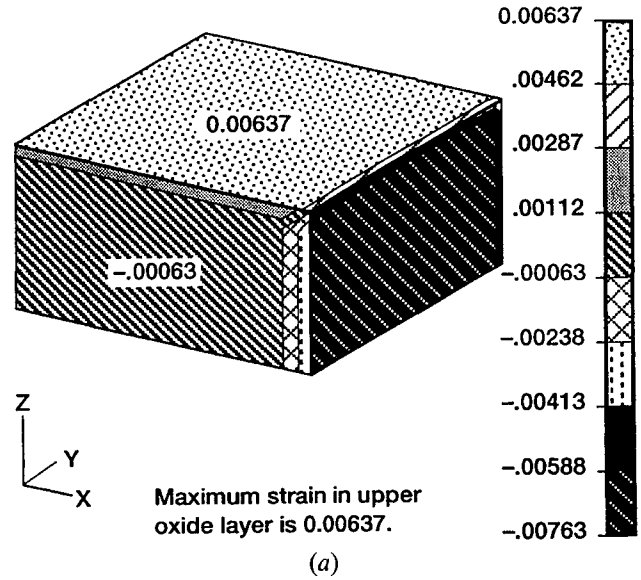

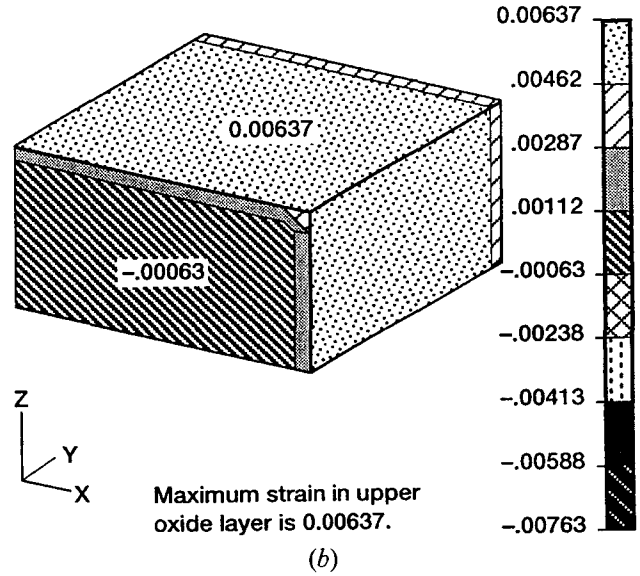

Fig. 14—The mechanical strains produced in the oxide layer and the MA956 plate by the CTE mismatch between the oxide and the MA956 under thermal cycling from 21 °C to 1204 °C: (a) mechanical x strain and (b) mechanical y strain.

for the y and z directions, but they would not add to the understanding gained so far. The strains in these other directions are important, however, because they are larger than the strain in the x direction. Figures 11(c) and (d) show the mechanical strain in the upper oxide layer for the y and z directions. The magnitudes of mechanical strain range are found to be 0.00397 and −0.00387, respectively. The inelastic stress-strain hysteresis loops for these two directions would be very similar, but obviously larger in strain range (by over 40 pct) to that in Figure 12 for the x direction. Because the maximum mechanical strain range in the oxide layer is in the y direction perpendicular to the fiber, the direction of greatest potential for oxide cracking will be perpendicular to this strain, *i.e.*, nominally parallel to the fiber in the x-z plane. This is in exact agreement with the experimental results of Figures 3 and 4. Close examination of Figures 4(b) and (c) also reveals progressive upheaval

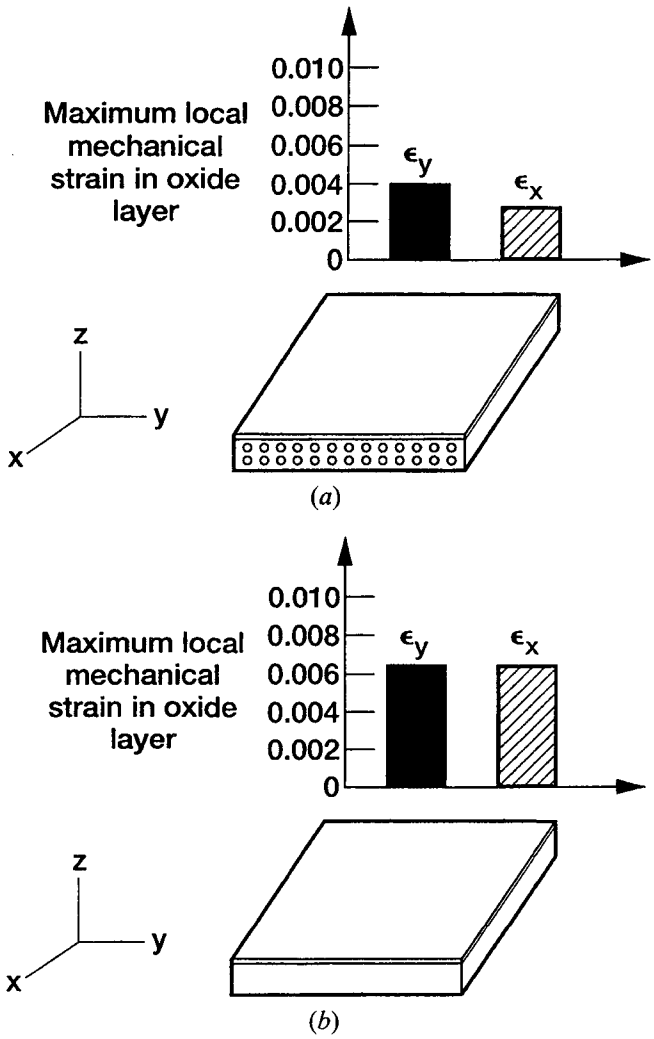

Fig. 15—Maximum mechanical strains in the oxide layer: (*a*) Sapphire/MA956 plate—unequal biaxial straining; and (*b*) MA956 plate—equibiaxial straining.

of material adjacent to each surface crack. This plastically upset material could only result from substantial inelastic compressive strains induced in the oxide during each cooldown portion of the thermal cycles. Such inelasticity has been shown by the analysis to be present, further demonstrating the understanding provided by the modeling efforts.

It is now necessary to examine some results for the unreinforced matrix plate with an oxide layer. The dimensions, loadings, *etc.* for the matrix plate are identical to those for the composite plate discussed previously and shown in Figure 10. The mechanical x and y strains produced in the oxide layer by the matrix plate due to CTE mismatch between the oxide and matrix materials are shown in Figure 14. The magnitudes and signs of the mechanical x and y strains are found to be 0.00637 (equibiaxial) in the oxide layer.* There is, thus, no preference for

*Because the unreinforced matrix has a higher CTE mismatch with the oxide layer than does the MMC, the magnitudes of mechanical strains in the oxide layer of the unreinforced matrix plate are appreciably higher than those for the oxide layer of the MMC plate. These results are summarized in Fig. 15, which depicts the magnitudes of maximum mechanical strains in the oxide layer of the MMC (Fig. 15(a)) and unreinforced matrix (Fig. 15(b)) plates.

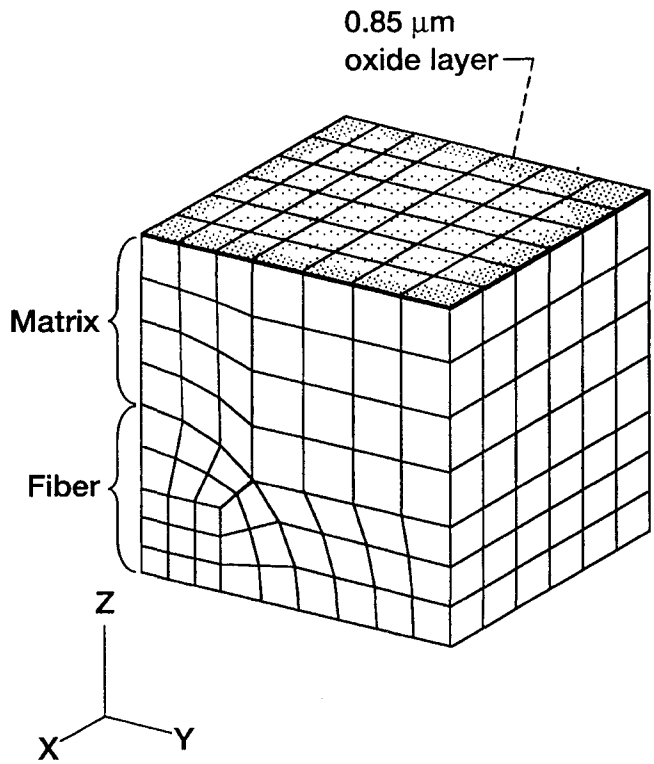

Fig. 16—The unit cell finite element model used for the micromechanical finite element analysis (450 elements, 658 nodes).

the cracking direction and, hence, random orientation of cracking would be expected. In fact, random crack orientation is what was observed for the thermally cycled coupons. The analytic modeling and the observations are in perfect qualitative agreement. The maximum thermally induced mechanical strain in the oxide layer of the unreinforced plate is much larger (between 1.6 and 2.3 times, depending upon direction) than that experienced in the oxide layer on the composite. Because of these considerably higher strains, there is an increased propensity for oxide cracking in tension during heating and subsequent oxide buckling (*i.e.*, popping out) and spallation during the cooldown portion of the cycle wherein the x-y plane of the oxide is placed in a highly compressed biaxial stress-strain state. It is to be noted that only the monolithic MA956 suffered from spallation. This is attributed to three factors: larger strains, random crack orientation, and the resultant closer oxide crack spacing for the monolithic coupons.

For the qualitative purposes of analytically predicting the direction and extent of cracking in the oxide layer (either composite or monolithic substrate), it was found acceptable to rely on (1) elastically computed mechanical *strain ranges*, (2) starting the stress-strain analysis at 21 °C, and (3) assuming zero initial residual stresses.

To analytically predict the location and spacing of cracking in the oxide layer for the composite coupons, it is necessary to resort to micromechanics analyses to examine the distribution of strains across the surface of the oxide.

C. *Micromechanical Finite Element Analyses*

Figure 16 shows the finite element model that was constructed to perform the micromechanical finite element

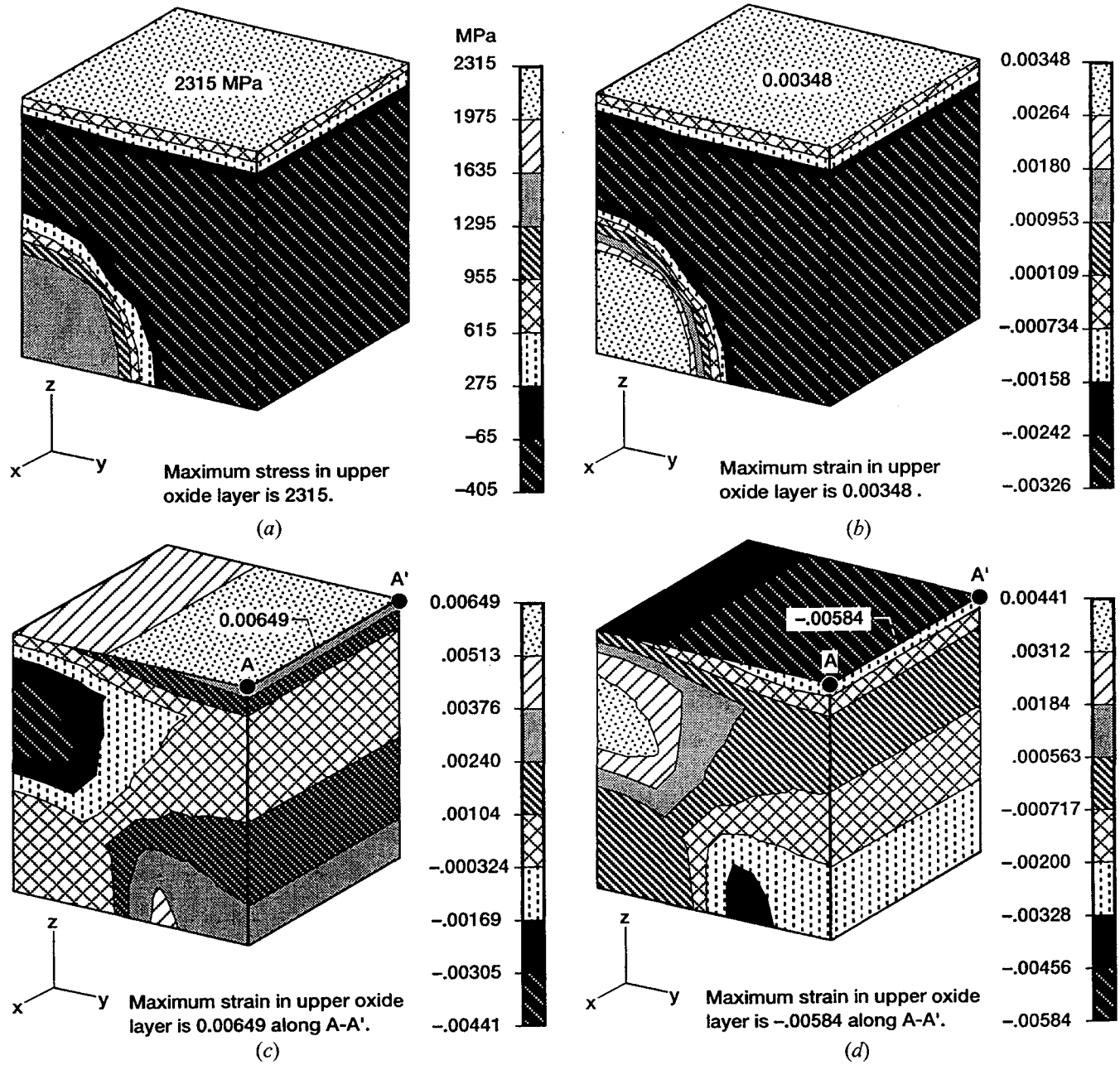

Fig. 17—The stress and mechanical strains in the oxide layer and Sapphire/MA956 composite unit cell: (*a*) *x* stress, (*b*) mechanical *x* strain, (*c*) mechanical *y* strain, and (*d*) mechanical *z* strain.

analyses. The unit cell model consists of one-quarter of a repeating volume element. The diameter of the fiber is 127 μm, and the fiber volume fraction is 0.35. The oxide layer, appearing only on the upper exposed surface, *i.e.*, perpendicular to the *z* direction, is also modeled. The 0.85-μm thickness of the oxide layer for the micromechanical model intentionally was selected to be considerably less than the thickness for the continuum model in order that the oxide layer not exert an undue influence on the significantly smaller volume and, hence, strength of the micromechanical unit cell. Fortunately, the precise choice of thickness is not crucial for the qualitative answers being sought. The most accurate value for thickness would have resulted in the same average stress in the oxide layer as was found for the macroscopic continuum mechanics analyses. The model consists of 450 solid, hexagonal elements and 658 nodes. Thermal exposure conditions were the same for the micromechanical model as for the continuum model.

The micromechanical finite element analyses were performed using the finite element program MARC. The temperature-dependent material properties of the constituents, *viz.* fiber, matrix, and oxide layer listed in Table III, were used in the analyses.

D. *Results of Micromechanical Finite Element Analyses*

Important results from these analyses are displayed in Figure 17. Note that the *x* direction continues to coincide

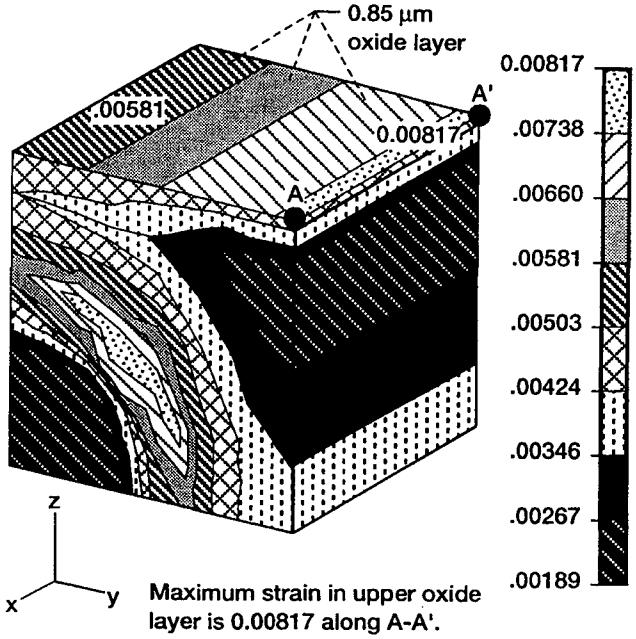

Fig. 18—The effective mechanical strain distribution in the Sapphire/MA956 composite unit cell.

with the fiber direction. Figure 17(a) shows the x-stress distribution in the MMC cell. As expected from the continuum analyses, the x stresses (and y and z stresses) were found to have magnitudes much higher than the yield strength of the oxide.* The strain values, on the other hand, are realistic as previously explained in the continuum analyses section.

*The magnitude of the x stress in the oxide layer obtained from the micromechanical analysis (Fig. 17(a)) is higher (2315 MPa) than obtained from the continuum analysis (1700 MPa, Fig. 11(a)). This is a result of having decreased the oxide thickness too much in order to keep it in proportion to the smaller dimensions of the unit cell. To achieve the proper thickness to keep the oxide stress constant at 1700 MPa would have required a time-consuming iterative process. Because the analyses were performed only to obtain qualitative results, higher quantitative accuracy was not required and, hence, not justified.

The mechanical x, y, and z strains in the MMC cell are displayed in Figures 17(b) through (d), respectively. From Figure 17(b) the maximum magnitude of the x strain produced in the oxide layer is tensile with a value of 0.00348. Figures 17(c) and (d) show the maximum mechanical y and z strains to also occur in the oxide layer, with respective magnitudes of 0.00649 and −0.00584. Comparing these figures, it is seen that the mechanical y strain has the maximum magnitude of all mechanical strains in the oxide layer. Furthermore, the location of the maximum mechanical y-strain magnitude is found to be in the valley, immediately above and halfway between adjacent fibers. The y-direction strain is the lowest immediately above the fiber. The effective (based on von Mises criteria) mechanical strain distribution in the MMC cell is exhibited in Figure 18. The effective strain is also found to have its maximum magnitude (0.00817) in the oxide layer at a location halfway between adjacent fibers. The direction of cracking caused by the effective strain is expected to be perpendicular to the direction (y) of the maximum principal strain. Thus, cracks should be expected to form in the oxide layer in the x-z plane perpendicular to the y strain and parallel to the fibers in the composite substrate. The resultant parallel cracks would be expected to have the same spacing as the fibers in the outer ply. Oxide spallation would be much less likely for this case because of the lack of intersecting oxide cracks. The analytic results are seen to be in agreement with and qualitatively support the experimental results shown in Figures 3 and 4.

V. SUMMARY AND CONCLUSIONS

MA956 exhibited a paralinear kinetics behavior, *i.e.*, parabolic weight gain followed by a linear weight loss, which is typical of alumina-forming alloys in cyclic oxidation. Scale cracking and spallation occurred in a random pattern, leading to the linear weight loss. Spallation occurred before cracks progressed into the MA956 substrate. In contrast, the parabolic kinetics of MA956/sapphire composite was followed by a linear weight gain without scale spallation. Massive uniform cracks parallel to the fiber axis developed which penetrated into the substrate. The linear weight gain was due to the increased oxidation surface created by the penetration of these cracks. Strong interfacial bonding combined with the large CTE mismatch contributed to the massive scale cracking in composites. Continuous removal of aluminum from the alloy eventually led to a breakaway oxidation, due to the rapid formation of iron oxide $(Fe,Cr)_2O_3$ in both MA956 and the composite.

Oxidative lifetime was calculated using the oxidation kinetics data. The aluminum content in the alloy at the beginning of breakaway oxidation was about 2.7 wt pct, which is a drop of 1.8 wt. pct from the initial content (4.5 wt pct). Lifetime of MA956 in the presence of scale spallation was substantially shorter than that for parabolic oxidation.

Results of the finite element analyses proved highly useful in providing understanding of the dissimilar cyclic oxidation cracking and spallation behavior of both the MA956 matrix material and the MA956/Sapphire fiber reinforced composite coupons. Analytic results accurately predicted the direction and location of cyclic oxidation cracking in both material systems.

ACKNOWLEDGMENT

We are grateful to Michael Maloney, Pratt and Whitney, for supplying the MA956 and Sapphire/MA956 composite materials.

REFERENCES

1. M.J. Donachie: in *Super Alloy Source Book*, M.J. Donachie, ed., ASM, Metals Park, OH, 1984, pp. 102-11.
2. J.S. Benjamin: in *New Materials by Mechanical Alloying Techniques*, E. Arzt and L. Schultz, eds., Verlag DGM, Oberursel, 1989, pp. 3-18.
3. K. Hilpert and M. Miller: *Z. Metallkd.*, 1992, vol. 83 (10), pp. 739-43.
4. D.P. Whittle and J. Stringer: *Phil. Trans. R. Soc. London A*, 1980, vol. 295, pp. 309-29.
5. A.W. Funkenbusch, J.G. Smeggil, and N.S. Bornstein: *Metall. Trans. A*, 1986, vol. 16A, pp. 923-32.
6. K.N. Lee and N.S. Jacobson: *Am. Ceram. Soc.*, 1995, vol. 78 (3), pp. 711-15.

7. J. Doychak, J.A. Nesbitt, R.D. Noebe, and R.R. Bowman: *Oxid. Met.*, 1992, vol. 38 (1–2), pp. 45-71.
8. D.B. Marshall and A.G. Evans: *J. Am. Ceram. Soc.*, 1985, vol. 68, pp. 225-31.
9. J.A. Nesbitt, R.R. Bowman, and S.L. Draper: *Hitemp Review*, NASA–Lewis Research Center, Cleveland, OH, 1994, vol. II, pp. 48:1-48:11.
10. K.N. Lee and Wayne L. Worrell: *Oxid. Met.*, 1994, vol. 41 (1–2), pp. 37-63.
11. W.J. Quadakkers and M.J. Bennett: *Mater. Sci. Technol.*, 1994, vol. 10, pp. 126-31.
12. W.J. Quadakkers and K. Bongartz: *Werk. Korros.*, 1994, vol. 45, pp. 232-41.
13. J.A. Nesbitt, E.J. Vinarcik, C.A. Barrett, and J. Doychak: *Mater. Sci. Eng.*, 1992, vol. A153, pp. 561-66.
14. C.E. Lowell, C.A. Barrett, R.W. Palmer, J.V. Auping, and H.B. Probst: *Oxid. Met.*, 1991, vol. 36 (1–2), pp. 81-112.
15. N. Birks and G.H. Meier: *Introduction to High Temperature Oxidation of Metals*, Edward Arnold, London, 1983, pp. 101-05.
16. A.J. Misra: *Scripta Metall. Mater.*, 1993, vol. 28, pp. 1189-94.
17. Y.S. Touloukian, R.K. Kirby, R.E. Taylor, and T.Y.R. Lee: *Thermophysical Properties of Matter*, IFI/Plenum, New York, NY, 1977, vol. 13.
18. Anon.: *MARC General Purpose Finite Element Program*, MARC Analysis Research Corporation, Palo Alto, CA, 1992, vol. A–D.
19. H.-J. Lee, P.K. Gotsis, P.L.N. Murthy, and D.A. Hopkins: *Metal Matrix Composite Analyzer (METCAN)*, User's Manual–Version 4.0, NASA TM-105244, NASA, Washington, DC, 1991.
20. J.B. Wachtman and L.H. Maxwell: *Am. Ceram. Soc.*, 1954, vol. 37 (7), pp. 291-99.
21. Anon.: *Engineering Properties of Ceramics*, AFML TR-66-52, AFML, Wright Patterson AFB, OH. 1966.